ACS APPLIED MATERIALS & INTERFACES

www.acsami.org Research Article

Controlled Heterovalent Vanadium Ion Coordinated Flower-Shaped Supramolecules Cathode for Zinc-Ion Storage

Yue Lu, Siyang Han, Jingang Zheng, Hongwei Zhao, Han Zhang, Guangshen Jiang, Lixiang Li, Weimin Zhou, Baigang An, and Chengguo Sun*

Cite This: *ACS Appl. Mater. Interfaces* 2025, 17, 1001−1013 Read Online

ACCESS | Metrics & More | Article Recommendations | Supporting Information

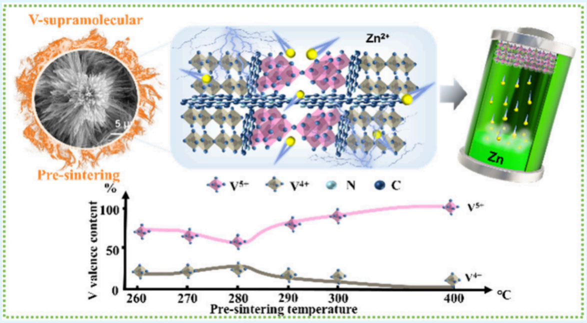

ABSTRACT: Vanadium-based materials, which offer multiple oxidation states and rich redox reactions in zinc-ion batteries (ZIBs), have gained substantial attention. However, achieving green and efficient preparation of vanadium oxides-based materials featured with a controlled content of different heterovalent vanadium remains a significant challenge. Herein, a vanadium-supramolecular flower-shaped material (VSF) with heterovalent vanadium was prepared using NH_4VO_3 as vanadium metal center and hexamethylenetetramine as organic ligand in aqueous solution. The optimal ratio of material (PVSF) after controlling VSF presintering is 2/1 (V^{5+}/V^{4+}). Employing PVSF-2/1 as cathode in ZIBs can achieve a high specific capacity of 398.9 mAh g^{-1} at 0.2 A g^{-1}, which is increased by 0.2 and 3.5 times as compared with that of pure VO_2 and V_2O_5, respectively. After 2000 cycles, it still delivers a specific capacity of 225 mAh g^{-1} at 5.0 A g^{-1}. The Zn||PVSF-2/1 pouch cells were assembled with a satisfactory specific capacity of 339 mAh g^{-1} at a current of 0.2 A g^{-1}. The excellent performance is ascribed to regulation and coordinated promotion of heterovalent states. The structural pathways corresponding to V^{5+} act as Zn^{2+} transport channels to increase Zn^{2+} transport capability. The V^{4+} cause high charge density distribution of the V-O lattice layer to provide abundant active sites for the adsorption/desorption process of Zn^{2+}.

KEYWORDS: *Zinc-ion batteries, Vanadium-supramolecular flower-shaped material, Regulating heterovalent vanadium, High specific capacity, Heterovalent states balance*

1. INTRODUCTION

Aqueous zinc-ion batteries (ZIBs) are projected to be the potential future of green rechargeable batteries due to their high safety, low-cost and facile manufacturing.[1,2] Like lithium-ion batteries (LIBs), the energy density of ZIBs is primarily determined by the cathode materials, in which the Zn^{2+} can be inserted into the host lattice.[3] Vanadium-based compounds with high reversible capacity, and long lifespan superior to that of other cathode materials, have gained huge consideration.[4] The multiple chemical valences of vanadium (V) element (+2 to +5) can not only achieve multiple electron transfers in redox reaction but also construct mixed valences of vanadium oxides materials (VOMs), such as vanadium oxides (V_2O_5, V_3O_7, V_6O_{13}), etc.[5,6] The diverse structural configuration and valence fluctuation of VOMs lead to differences in the zinc-ions storage mechanism including the Zn^{2+} insertion mechanism and H^+/Zn^{2+} co-insertion mechanism, thereby resulting in huge differences in electrochemical performances.[7] Actually, the capacity and rate performance of vanadium-based cathodes applied to ZIBs have always been incapable of achieving satisfactory performance owing to deficient electrochemical reaction aroused by inferior electrical conductivity, vanadium dissolution and high steric resistance and electrostatic repulsion.[4,8,9]

To address the issues, much effort has been devoted to modulate the morphology,[10] such as constructing conductive skeleton composites,[11] introducing heterogeneous atoms,[12] expanding the lattice spacing[13] and creating vacancy of vanadium-based materials for vanadium-based cathodes.[14] Interestingly, we found all designed vanadium-based materials with mixed-valence configuration, and the related literature primarily indicated that mixed valence states contribute to high capacity, fast ion diffusion kinetics and low polarization over single V^{5+}.[15,16] For example, partial V^{5+} ions in $NH_4V_4O_{10}$ cathode materials are reduced to V^{4+} after the insertion of potassium ion, resulting in a high discharge specific capacity of 464 mAh g^{-1} at 0.1 A g^{-1}.[17] The mixed-valence of V^{4+} and V^{5+} in the V_2O_5/V_6O_{13} heterostructure delivered a diffusion energy

Received: September 23, 2024
Revised: December 6, 2024
Accepted: December 8, 2024
Published: December 20, 2024

https://doi.org/10.1021/acsami.4c16336

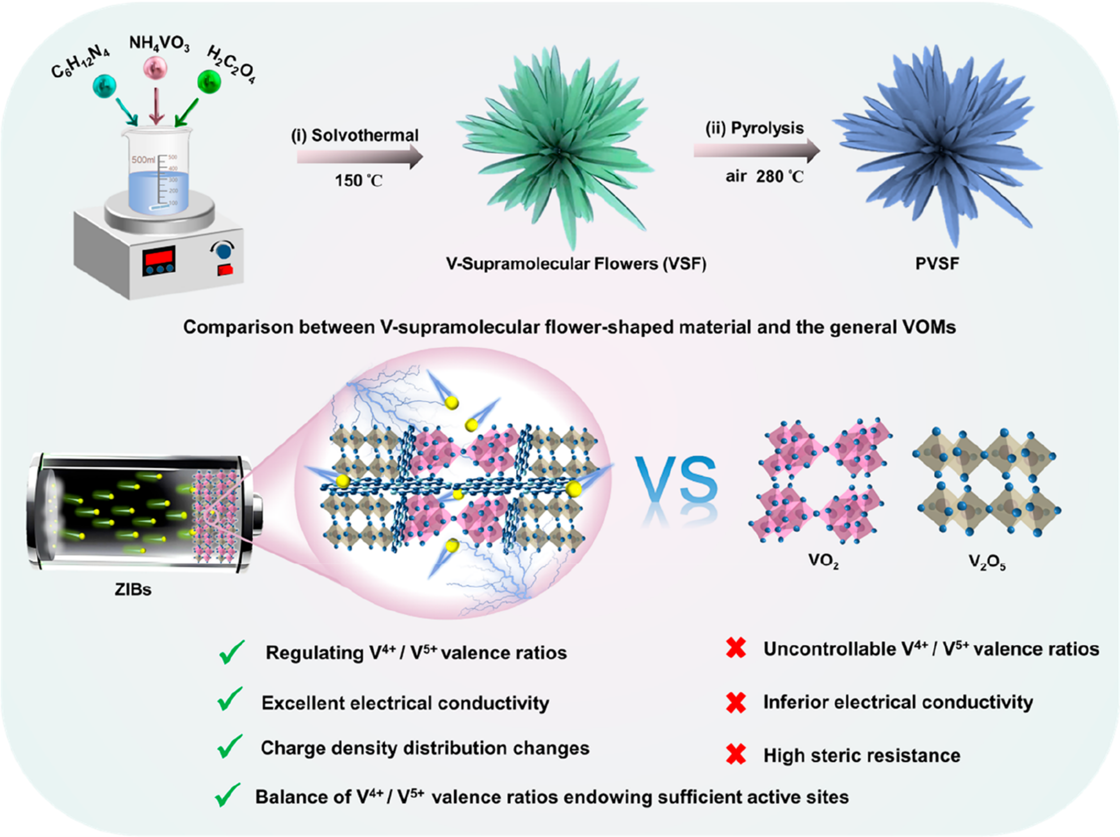

Figure 1. Schematic diagram of the preparation procedure for PVSF with different heterovalent ratios V^{5+}/V^{4+} by a simple presintering treatment in air.

barrier of Zn^{2+} to be 0.74 eV, much lower than that of V_2O_5 (1.20 eV), further demonstrating the rapid Zn^{2+} diffusion in the mixed-valence states V_2O_5/V_6O_{13} heterostructure.[18,19] The cyclic voltammetry curve of V^{4+}-V_2O_5 shows a smaller gap (130 mV) between the redox peaks than that of V_2O_5, illustrating the lower polarization of V^{4+}-V_2O_5.[16] The above-mentioned achievements prove that the formation of mixed-valence material leads to outstanding electrochemical properties. However, the effect of different valence ratios on ZIBs performances is confusing, and few detailed methods for controllably preparing mixed-valence materials have been reported. Most literature indicated that constructing vanadium-based materials with uniform structural morphology typically suffers from high temperatures (≥180 °C) and extended reaction time (≥24 h) at a high pressure.[20−22] Therefore, achieving the facile preparation of VOMs featuring a regulated content of different vanadium valences remains of practical interest.[23,24]

Inspired by the above research reports, herein, we synthesized a vanadium-supramolecular flower-shaped material (VSF) via a hydrothermal method using NH_4VO_3 as the metal center of vanadium and hexamethylenetetramine ($C_6H_{12}N_4$) as the organic ligand. After presintering at a temperature ranging from 260 to 400 °C, flower-shaped vanadium-based materials with different heterovalent ratios of V^{4+} and V^{5+} were obtained. By optimizing the V^{5+}/V^{4+} ratios to 2:1, the PVSF-2/1 material with a balance of the heterovalent states was achieved. Using PVSF-2/1 as a cathode of aqueous ZIBs can achieve high specific capacity (398.9 mAh g^{-1} at 0.2 A g^{-1}), remarkable rate capability, and excellent cycling lifespan. The excellent properties of PVSF-2/1 can probably be attributed to the heterovalent balance of PVSF-2/1 that the structural pathways corresponding to V^{5+} valence work as Zn^{2+} transport channels to increase Zn^{2+} transport capability and V^{4+} valence causes the high charge density distribution of the V-O lattice layer to provide rich active sites for the adsorption and desorption process of Zn^{2+}. The unique flower-shaped structure of PVSF-2/1 contributes to efficient charge transfer and high ion diffusion ability ($D_{Zn^{2+}} = 10^{-9}$−10^{-10} cm^2 s^{-1}). In addition, a H^+/Zn^{2+} co-insertion mechanism for the PVSF-2/1 cathode is verified by an ex-situ characterization technique. This work provides a valuable design strategy from the perspective of controlling the valence of vanadium for the development of high performance ZIBs cathode materials.

2. EXPERIMENTAL SECTION

Materials. Vanadate ammonium (NH_4VO_3) was purchased from the official Web site of McLean Reagent. Oxalic acid ($H_2C_2O_4$) was purchased from the discovery Platform. A Whatman glass fiber membrane was purchased from DoDochem Co., Ltd. Zn foil and Ti foil were purchased from Teng feng Metal Materials Co., Ltd. Other chemical materials were purchased from Sinopharm Chemical Reagent Company. All chemical materials were directly used without purification.

Preparation of Flower-Shaped Vanadium-Supramolecules and PVSF-2/1. First, 1.23 g of NH_4VO_3 and 0.31 g of $C_6H_{12}N_4$ were dissolved into a beaker containing 20 mL of deionized water and were stirred vigorously for 10 min. Second, 2.62 g of $H_2C_2O_4$ was poured into the beaker until the homogeneous liquid turned into a yellow transparent solution, followed by a dark green color after about 20 min of stirring. Then, the solution was transferred into a Teflon-lined stainless teel autoclave and kept at 150 °C for 1 h. The flower-shaped V-supramolecules were prepared via suction filtration and were dried

https://doi.org/10.1021/acsami.4c16336
ACS Appl. Mater. Interfaces 2025, 17, 1001−1013

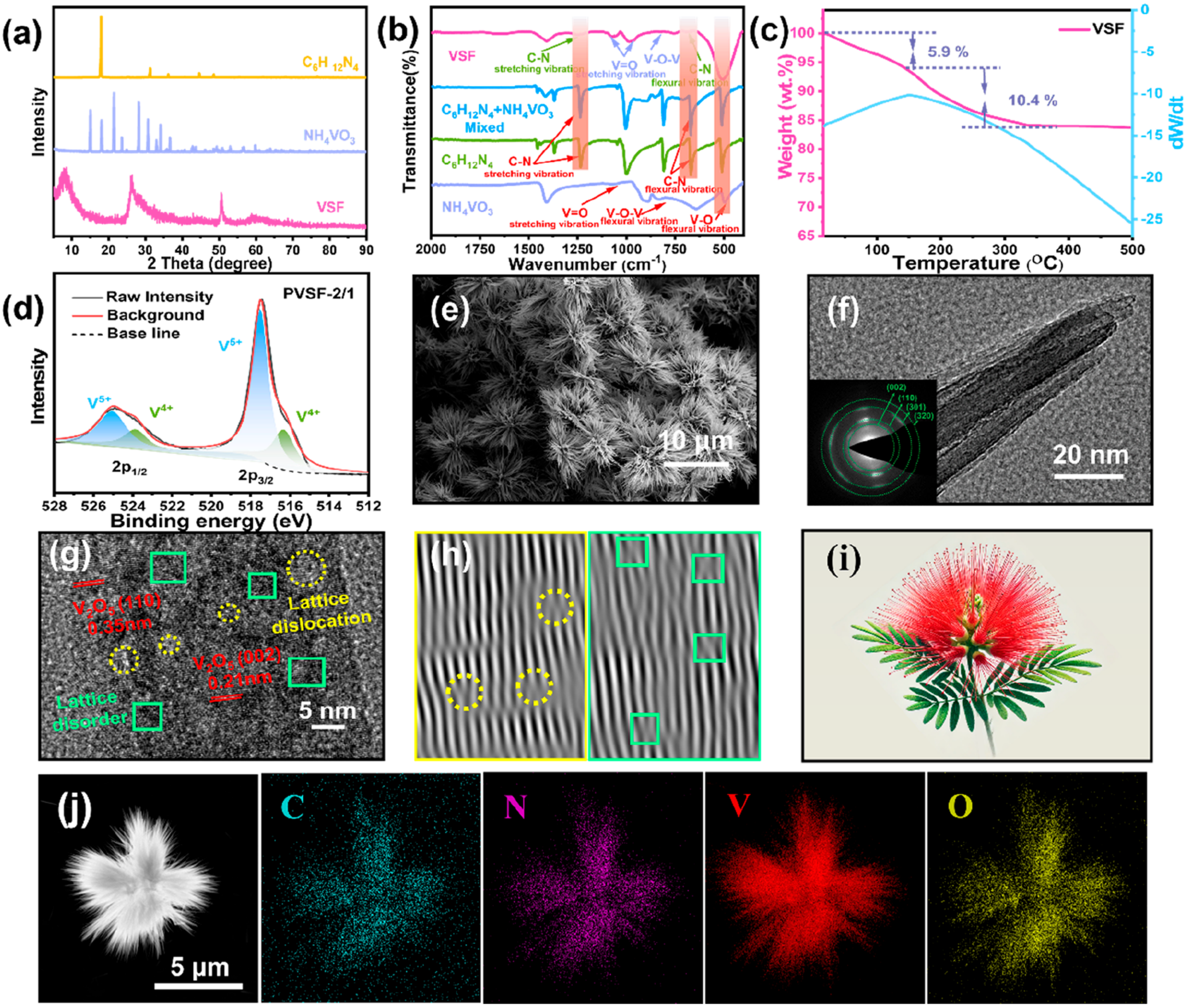

Figure 2. (a) XRD patterns of $C_6H_{12}N_4$, NH_4VO_3 and VSF. (b) FTIR spectra. (c) TG curves of VSF. (d) XPS characterization of the V 2p spectra for PVSF-2/1. (e) SEM image of PVSF-2/1. (f) TEM and (g) HRTEM images of PVSF-2/1; Inset: the selected area electron diffraction (SAED) pattern. (h) Corresponding IFFT images. (i) Schematic diagram of calliandra hematocephala hassk. (j) HAADF-STEM images of PVSF-2/1 and corresponding elemental mapping of C, N, V and O, respectively.

at 50 °C in vacuum. PVSF-2/1 was obtained by annealing the V-supramolecules in an air atmosphere for 2 h at 280 °C with a heating rate of 2 °C min^{-1}. V_2O_5 with pure pentavalent vanadium can be obtained at temperatures above 400 °C.

Characterizations. The morphologies, composition, and structure of products were characterized by SEM (Apreos), TEM (Tecnai G2 F20), XRD (D/Max2500 with Cu Ka radiation), FT-IR (EQUINOX55), BET method N_2 adsorption isotherm (ASAP-2020), Raman (HORIBA Xplora Plus),electron paramagnetic resonance (EPR, A300-10/12) and XPS (Kratos A XIS-SUPRA).

Electrochemical Characterization. The electrochemical properties of the as-prepared PVSF and comparative samples were tested via CR2025 coin cells. The cathode electrodes were fabricated by coating a Ti foil with a slurry mix, which consisted of active material (70 wt %), acetylene black (20 wt %), and poly(vinylidene fluoride) binder (10 wt %) mixed in *N*-methyl-2-pyrrolidone (NMP) solution, with drying in a vacuum oven at 80 °C for 12 h. Zinc foil was utilized as anode, and a 2 M $ZnSO_4$ aqueous solution was employed as electrolyte, and a glass fiber filter as separator. The mass loading of active materials on the electrode was approximately 1−1.5 mg cm^{-2}. The electrochemical behavior was evaluated at voltages between 0.2 and 1.5 V. Galvanostatic charge/discharge tests and the galvanostatic intermittent titration technique (GITT) were carried out with a multichannel battery testing system (LAND CT2001A). Cyclic voltammetry (CV) tests were carried out with a Bio-Logic six-channel electrochemical workstation, France. Electrochemical impedance spectrometry (EIS) measurements were performed in the frequency range of 100 kHz to 10 mHz on a Bio-Logic six-channel electrochemical workstation, France. All the electrochemical measurements were carried out at a controlled room temperature of 25 °C. Assembly of pouch Zn-ion batteries was undertaken using 4.2 cm × 4.2 cm PAM/$ZnSO_4$ hydrogel electrolyte as the separator, 4 cm × 4 cm Zn foil as anode and 4 cm × 4 cm PVSF-2/1 as the cathode.

3. RESULTS AND DISCUSSION

The vanadium-supramolecular flower-like material (VSF) was synthesized via a one-step hydrothermal method. As shown in Figure 1, NH_4VO_3 as the sacrificial precursor is reduced by $H_2C_2O_4$ in solution to form V-ion complexes; subsequently, in the presence of hexamethylenetetramine, VSF was formed via the hydrogen bonding self-assembly technique (Figure S1). To regulate the heterovalent states (V^{5+}/V^{4+}) balance of flower-shaped vanadium-supramolecule materials, the VSF sample was treated with an air presintering process by controlling temperature ranging from 260 to 400 °C. V^{5+}/V^{4+} heterovalent ratios of 2:1, 3:1, 4.5:1 and 100:1 in pyrolytic VSF (PVSF) were achieved.

X-ray diffraction (XRD) was evaluated to determine the crystal component. In contrast to NH_4VO_3 and $C_6H_{12}N_4$, it can be found that the VSF has four obvious peaks at 8.2, 26.2, 50.7 and 60.5° (Figure 2a). The appearance of new peaks in the vanadium-supramolecule material is strong evidence for new substances generation. After heat treatment at 280 °C, the sintered vanadium-supramolecule material has weak crystallinity with typical peaks located at 26.2°, 31.8°, 47.3°, and 60.5°, corresponding to the (110), (301), (600), and (321) planes of V_2O_5 (orthorhombic, JCPDS card no. JCPD41-1426), respectively (Figure S2a). Interestingly, an obvious characteristic peak was observed at 50.7° for PVSF-2/1. It was attributed to vanadium valence oxidation during hydrothermal and presintering processes, which led to the formation of heterovalent VO_x lattice planes, thus forming the heterovalent form of PVSF. To explore the effect of temperature on the crystal composition, the VSF was pyrolyzed at temperature between 260 and 400 °C in air. As shown in Figure S2b, we found that the peak position and intensity remain consistent at sintering temperature ranging from 260 to 285 °C, indicating that the low temperature was unable to cause significant structure changes of VSF. When the sintering temperature exceeds 290 °C, an obvious peak assigned to V_2O_5 appeared, illustrating that the highly crystalline V_2O_5 was formed in PVSF.

Further evidence for the formation of VSF is achieved by Fourier transform infrared spectroscopy (Figures 2b and S2c). Taking $C_6H_{12}N_4$, NH_4VO_3 and their mixtures as contrast samples, the disappearance of the stretching vibration bands of N-H (νNH_2) at near 3185 cm^{-1} indicates the interaction between NH_4VO_3 and $C_6H_{12}N_4$, indicative of the presence of hydrogen bonding in the VSF (Figure S2c).[25,26] Besides, in contrast to their mixtures, the peaks located at 1235 and 656 cm^{-1}, assigned to the stretching vibration and flexural vibration of C-N, shift to 1254 and 676 cm^{-1} higher wavenumbers in coordination polymer VSF, which proves the interaction between $C_6H_{12}N_4$ and NH_4VO_3 to form VSF (Figure 2b).[20] The characteristic peak of 493 cm^{-1} belongs to the flexural vibration of V-O in NH_4VO_3, and a redshift toward the long-wave direction to 503 cm^{-1} in VSF is caused by vanadium valence oxidation during the hydrothermal process. As for VSF, the new peaks located at 830 and 1060 cm^{-1} are ascribed to the flexural vibration response of V-O-V,[27] and the stretching vibration response of V═O.[17,28]

The thermostability of VSF was investigated by Thermo-Gravimetry (TG) (Figures 2c and S2d). The mass loss could be divided into two processes: the first mass loss of 5.9 wt % below 150 °C is due to the loss of free/crystal water in VSF. The second process was completed at about 350 °C with 10.4 wt % weight loss, which can be attributed to the decomposition of NH_4VO_3 and $C_6H_{12}N_4$. The results indicated the composition and presintering processes of VSF polymer.

To further analyze the valence status of vanadium element in VSF and PVSF, the survey XPS spectra confirmed the four distinct peaks of C, N, V, and O elements (Figure S2e). Figure S3a displays the high-resolution spectrum V 2p of VSF, which can be classified as 517.5 and 525.3 eV for V^{5+} $2p_{3/2}$ and $2p_{1/2}$, while the two peaks at 516.3 and 524.6 eV were divided as V^{4+} $2p_{3/2}$ and $2p_{1/2}$, respectively.[16,29] The heterovalent ratio V^{5+}/V^{4+} of VSF was calculated to be 2.2:1 by fitting the split peaks area of V^{5+} and V^{4+}. It is worth noting that the abundant V^{4+} is derived from V^{5+} valence reduction during 150 °C hydrothermal processes. According to the TG curves of VSF and $C_6H_{12}N_4$, the sintering experiments were conducted at temperatures ranging from 260 to 400 °C, the corresponding XPS spectrum of PVSF with different heterovalent ratios V^{5+}/V^{4+} can be found in Figure S3, and the details of presintering temperature and V^{5+}/V^{4+} heterovalent ratios of PVSF are shown in Table S1. We concluded that with sintering temperature increases from 260 to 400 °C, the V^{5+} content in PVSF is generally increased, with the corresponding obvious reduction in the V^{4+} content. At a temperature of 400 °C, only V^{5+} was found in PVSF (labeled as PVSF-100). At other temperatures, the different heterovalent ratios V^{5+}/V^{4+} in PVSF are labeled as PVSF-3/1, PVSF-2.5/1, PVSF-2/1, PVSF-3.5/1 and PVSF-4.5/1, corresponding to 260, 270, 280, 290, and 300 °C, respectively. During the above conversion process of vanadium valence states, the content relative to V^{4+} reflected a volcano type of variation trend, which can reach a maximum content of 33.9% for V^{4+} and a minimum content of 66.1% for V^{5+} at 280 °C (Figure 2d). The valence ratio V^{5+}/V^{4+} of PVSF was calculated to be 2:1. The results indicate the decomposition of NH_4VO_3 to form V_2O_4 during 280 °C. When the temperature exceeds 280 °C, V^{4+} gradually transforms to V^{5+} until the PVSF is completely converted to V_2O_5 at 400 °C. Further evidence can be verified by XRD results. The O 1s spectrum of VSF was resolved into three components of lattice oxygen (O1), oxygen vacancies (O2) and H_2O molecule (O3) at 529.7, 530.6, and 532.3 eV, respectively (Figure S4).[14,17,30,31] The visibly stronger O2 peak of PVSF is observed, demonstrating that the decomposition of NH_4VO_3 leads to vanadium valence state changes and is also accompanied by generation of oxygen defects during presintering. Therefore, different V^{5+}/V^{4+} heterovalent ratios from 260 to 400 °C also result in different degrees of oxygen vacancies, which are 15.1, 19.6, 21.7, 18.7, and 16.5%, respectively. We conclude that PVSF-2/1 with a V^{5+}/V^{4+} heterovalent ratio of 2:1 has the largest O2 content of 21.7% (Table S2).

The oxygen vacancies were also confirmed by the electron paramagnetic resonance spectra (EPR) on the basis of the unpaired electrons.[32] The V^{4+} is paramagnetic because of the unpaired electrons, while V^{5+} is EPR signal silent owing to the integer spin. Therefore, the EPR peak intensity reflects a V^{4+} valence signal and concentration of oxygen vacancy state.[33] As shown in Figure S5, a strong EPR signal at g = 2.003 for V^{4+} appeared in both PVSF and VSF, with a higher peak intensity of PVSF than that of VSF, indicating that V^{5+}/V^{4+} heterovalent ratios can be regulated during the presintering process. This is in accordance with the XPS results.

Scanning electron microscopy (SEM) and TEM images display the flower-shaped structure of VSF with a uniform size of around 10 μm (Figure S6a, b). After calcination at 280 °C, the petals of PVSF-2/1 were transformed from the original two-dimensional micrometer sheet into a finer two-dimensional nanosheet (Figures 2e and S6c, d). To further understand the microstructure of PVSF-2/1, we performed TEM tests on a single PVSF-2/1 petal. Figure 2f shows that the uniform width of each petal is approximately 25 nm. The high-

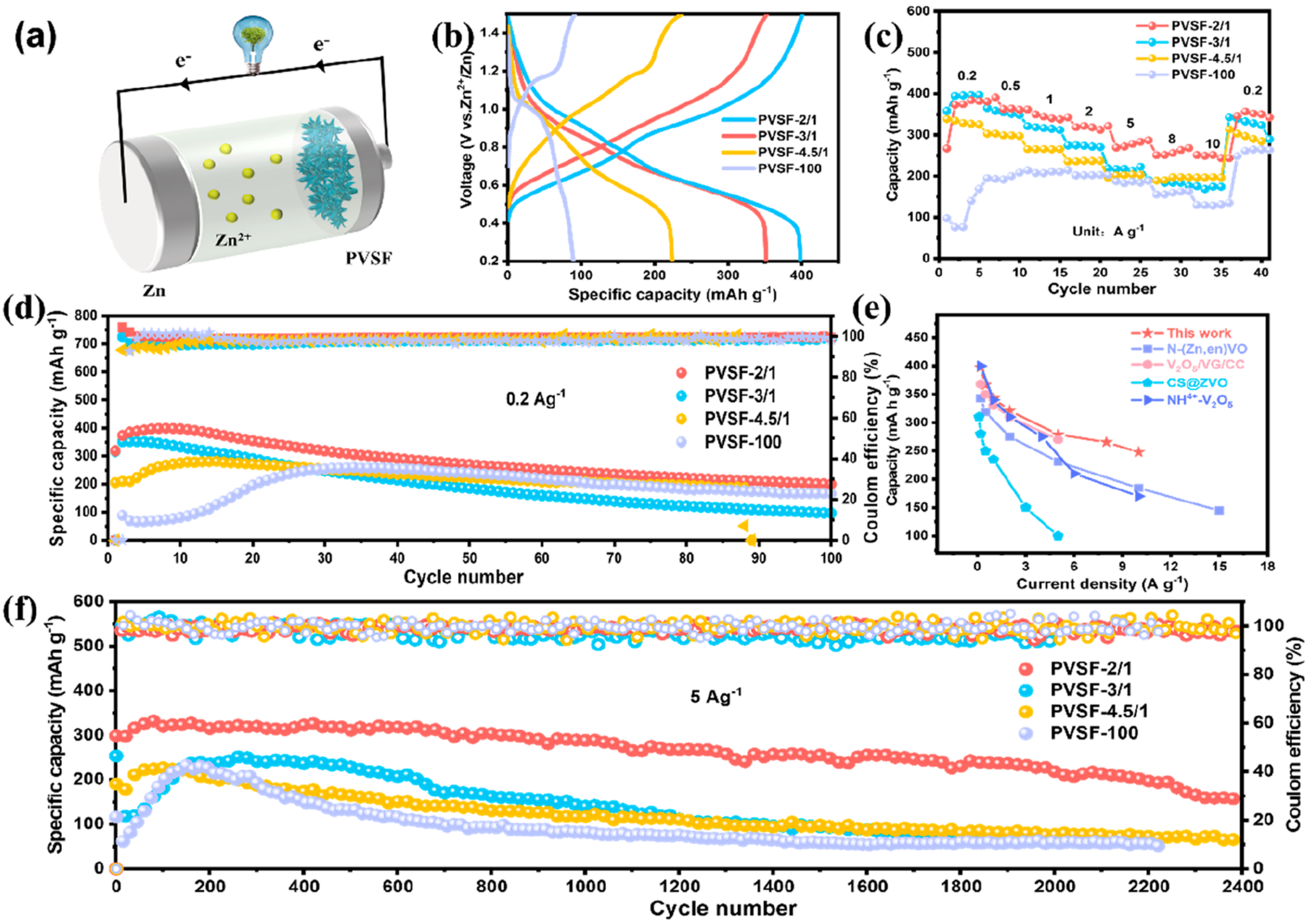

Figure 3. (a) Schematic depicts the PVSF as a cathode in aqueous ZIBs device. (b) Galvanostatic charge/discharge (GCD) plots of PVSF cathodes with different heterovalent ratios at 0.2 A g^{-1}. (c) Rate performance. (d) Cycling stability of PVSF cathodes with different heterovalent ratios at 0.2 A g^{-1}. (e) Ragone plots of PVSF cathodes in aqueous ZIBs with other types of cathode materials. (f) Long-cycling stability of PVSF cathodes with different heterovalent ratios at 5.0 A g^{-1}.

resolution TEM image (HRTEM) of PVSF-2/1 distinctly demonstrates that the lattice spaces of 0.35 and 0.21 nm indexed to the V_2O_5 (110) plane and V_2O_5 (002) plane, respectively.[34] Figure 2g also shows various lattice spacing disorders and lattice spacing dislocations induced by heterovalent changes. The corresponding inverse Fourier transform (IFFT) images confirm the lattice spacing disorder and dislocation (Figure 2h). The selected area electron diffraction (SAED) patten displays the regular diffraction rings of PVSF-2/1. It shows four diffraction rings indexed to the (002), (110), (301) and (320) planes of V_2O_5, indicating that polycrystalline property of the PVSF-2/1 (Inset in Figure 2f). HAADF-STEM images show that four elements (C, N, V, and O) are evenly distributed in the entire micrometer-flower (Figure 2j) as well as the four elements observed from the X-ray energy-dispersive spectrum (EDS) (Figure S7). In light of the shape and appearance, the morphology of PVSF-2/1 was very similar to that of natural calliandra hematocephala hassk (Figure 2i). Especially at the sintering temperature ranging from 260 to 300 °C, the PVSF morphology can maintain the flower-shaped pattern. However, the V^{5+}/V^{4+} heterovalent ratios change obviously and can be regulated by controlling the sintering temperature (Figure S8).

According to the nitrogen-adsorption/desorption test revealed in Figures S9 and Table S3, the VSF sample exhibits a specific surface area of 11.3 m^2 g^{-1} and an average pore size of 22.9 nm. After presintering, PVSF-2/1 has the higher specific surface area of 20.7 m^2 g^{-1} and average pore size of 17.7 nm. The increase of specific surface areas is attributed to the decomposition and oxidation of $C_6H_{12}N_4$ in VSF during sintering. Such micron-flower petals with unique structural features of thin two-dimensional porous nanosheets are predicted to effectively expose more active sites for favoring zinc salt electrolyte penetration and Zn^{2+} transport.[20,35]

To evaluate the electrochemical properties of PVSF electrodes with different heterovalent ratios (V^{5+}/V^{4+}), coin-type ZIBs were assembled with zinc foil as the anode, PVSF cathode material, and aqueous 2 M $ZnSO_4$ solution as the electrolyte (Figure 3a). The redox process of the PVSF-2/1 cathode was confirmed by cyclic voltammetry test (CV) in the voltage range of 0.2−1.5 V at a scan speed of 0.2 mV s^{-1} (Figure S10a). Two couples of oxidation and deoxidation peaks at 0.564/0.808 V and 0.947/1.176 V appeared and are related to the vanadium valence conversion relation and insertion of H^+ ions.[36,37] For three cycles, the two oxidation peaks shifted to the left, and two reduction peaks shifted to the right, which are 0.585/0.785 V and 1.016/1.151 V, respectively. This phenomenon is mainly caused by the activation process that can narrow the redox potential window.[30,38] The gradual symmetry of the typical redox

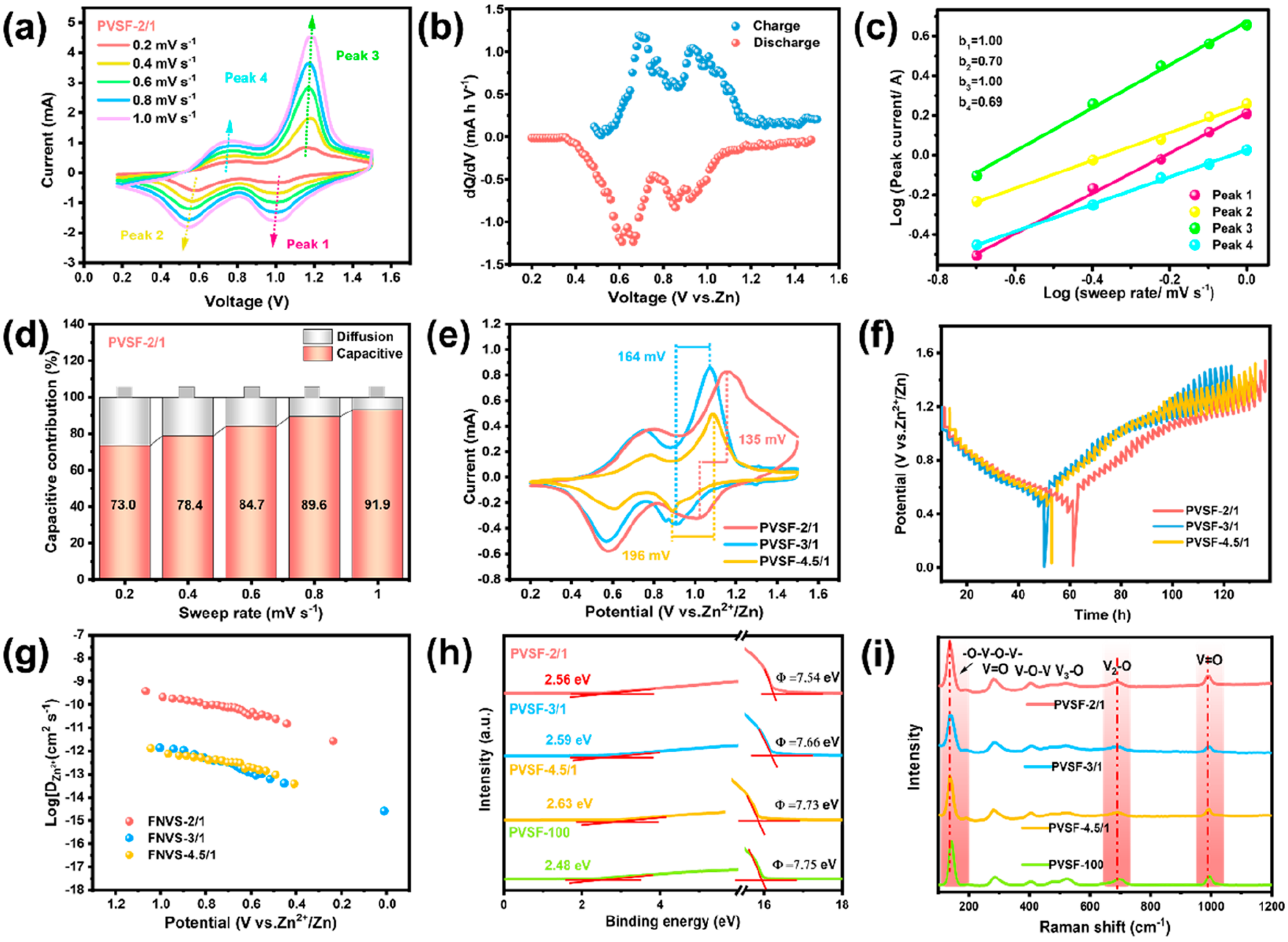

Figure 4. (a) CV curves of PVSF-2/1 electrode at various scan rates. (b) dQ/dV curve of the PVSF-2/1 for the 10th cycle at 0.2 A g^{-1}. (c) Log (peak current) versus log (sweep rate) plots according to the CV data at selected oxidation/reduction peaks. (d) Capacitive contributions of PVSF-2/1 at different scan rates. (e) CV curves of PVSF electrodes with different heterovalent ratios at 0.2 mV s^{-1}. (f) Charge−discharge curves in the GITT measurement of PVSF electrodes with different heterovalent ratios at 0.2 A g^{-1}. (g) Calculation of the Zn^{2+} diffusion coefficient of PVSF electrodes with different heterovalent ratios at various discharge. (h) UPS spectra. (i) Raman spectra of PVSF with different heterovalent ratios.

peaks illustrates the increased reversibility and stability. The PVSF-3/1, PVSF-4.5/1 and PVSF-100 cathodes also show two pairs of redox peaks (Figure S10b−d), all of which locate at similar redox potential range to that of PVSF-2/1 except for the lower peak current densities. The results imply that controlling the heterovalent ratio (V^{5+}/V^{4+}) to 2:1 in PVSF by presintering has superior electrochemical reactivity and capacity to other ratios.[16]

The galvanostatic charge−discharge (GCD) profiles of the PVSF-2/1 cathode for the initial ten cycles at a current density of 0.2 A g^{-1} are shown in Figure S10e. It is easy to note that the GCD profiles overlap perfectly, demonstrating great reversibility and structural stability. Moreover, the voltage plateau reveals a potential similar to that of the oxidation and deoxidation peaks of the CV curve in PVSF-2/1. In contrast to PVSF-3/1, PVSF-4.5/1 and PVSF-100, the GCD curve of the PVSF-2/1 cathode exhibits the maximum discharge capacity of 398.9 mAh g^{-1}, which was expressively better than the discharge capacities of 352.5, 236.6, and 89.3 mAh g^{-1} for the PVSF-3/1, PVSF-4/1, and PVSF-5/1 cathodes, respectively (Figure 3b). Controlling the V^{5+}/V^{4+} heterovalent ratio to 2/1 boosts the capacity by 4.5 times compared with that of PVSF-100, only containing V^{5+}. Figure 3c further evaluates the rate performance of PVSF with different heterovalent ratios. The PVSF-2/1 delivers the high reversible capacities of 398.9, 363.9, 344.5, 321.5, 283.2, and 251.4 mAh g^{-1} at the current densities of 0.2, 0.5, 1.0, 2.0, 5.0, and 8.0 A g^{-1}, respectively. Even at a high current density of 10 A g^{-1}, PVSF-2/1 also maintains a high specific capacity of 243.7 mAh g^{-1} (Figure S10f), which is much larger than those of PVSF-3/1 (172.2 mAh g^{-1}), PVSF-4.5/1 (193.1 mAh g^{-1}) and PVSF-100 (133.4 mAh g^{-1}). When the current density reverts to 0.2 A g^{-1}, the specific capacity can be recovered, indicating good cycle stability of the PVSF-2/1 cathode. The performance of PVSF-2/1 is compared with other different reported vanadium oxides-based cathodes in ZIBs (Table S4). Obviously, the PVSF-2/1 with a balance of V^{5+}/V^{4+} heterovalent ratios indicates larger capacity and superior rate capability than those reported cathode materials without valence regulation (Figure 3e).[16,39] This is mainly due to the regulated vanadium heterovalent ratios; the heterovalent balance of V^{5+}/V^{4+} ratios can improve the charge density distribution of V-O lattice layers, endowing sufficient active sites as well as ensuring the adsorption and desorption process of Zn^{2+} during the reaction process.[26,40] To evaluate the long-cycling capability of the Zn-PVSF battery, GCD curves at 0.2 and 5.0 A g^{-1} were conducted. The capacity retention of PVSF-2/1 is about 63% after 100 cycles at 0.2 A g^{-1} (Figure 3d). The degeneration of capacity may be attributed to structure changes upon Zn^{2+} insertion and sequential V-O lattice distortion and loss of active sites.[41,42] The PVSF-2/1 can still preserve ∼78.5% capacity retention after 2000 cycles at 5.0 A g^{-1}, which is higher than those of other prepared cathodes (∼26.1%, ∼34.8%, and ∼25.4% for PVSF-3/1, PVSF-4.5/1, and PVSF-100, respectively) (Figure 3f). Note that the Coulombic efficiency for PVSF-2/1 is approximately 100%, further revealing the superior reversibility and remarkable long-term cycling lifespan.

The multiple chemical valences of vanadium with more achievable Zn^{2+} insertion are responsible for the considerable specific capacity. To determine the capacity current distribution with diffusion or faradaic contribution, the CV curve was studied at various scan rates of 0.2−1 mV s^{-1} to reveal the electrochemical kinetics process of PVSF with different heterovalent ratios (Figures 4a and S11,12). All CV profiles of PVSF with different heterovalent ratios exhibit two pairs of oxidation/reduction peaks corresponding to two-step Zn^{2+} insertion/extraction processes.[43] The CV profiles maintained a similar shape at increased scan rates, indicating the PVSF electrode tolerance to Zn^{2+} insertion/extraction.[44] The negligible redox peak shift is ascribed to the polarization during Zn^{2+} insertion/extraction.[45] Moreover, the differential capacity (dQ/dV) curves exhibited two pairs of broad peaks (10th cycle) (Figure 4b), consistent with the CV results. The high capacity of PVSF-2/1 is attributed to regulating the vanadium heterovalent ratios. The similar shape of curves with negligible shift from 30th to 80th cycle further proved the excellent stability of PVSF (Figure S13). The capacitance response of the battery was determined via the linear relationship of eq 1 between the peak current (i) and scan rate (v). The mentioned relationship can be slightly rearranged to eq 2:[46]

$$i = av^{b} \tag{1}$$

$$\log(j) = b\log(v) + \log(\mathrm{a}) \tag{2}$$

where a and b represent adjustable parameters.[47] When the fitted b value is close to 0.5, the electrochemical reaction process relies on ionic diffusion control. When the fitted b value approaches 1.0, the reaction process is dominated by thefaradaic contribution.[48] Based on eqs 1 and 2, the b values for the four main redox peaks can be calculated to be 1.00, 0.70, 1.00, and 0.69, respectively (Figure 4c). Thus, the charge storage process is affected by a mixed contribution of controlled ionic diffusion and faradaic capacitive. In the high-voltage phase, the electrochemical reaction process possesses faradaic capacitance behavior, whereas ion diffusion behavior affects the electrochemical reaction process during the low-voltage range. This renders good Zn^{2+} diffusion kinetics. Additionally, the detailed capacitive contribution percentages can be calculated via the following eqs 3 and 4:

$$i = k_1 v + k_2 v^{1/2} \tag{3}$$

$$iv^{1/2} = k_1 v^{1/2} + k_2 \tag{4}$$

where k_1 and $k_2 v^{1/2}$ denote the contributions of the diffusion effects and the faradaic capacitance behavior, respectively.[49] With the sweep rates from 0.2 to 1 mV s^{-1}, the percentage of the capacitance contribution increases from 73.0% to 91.9% (Figure 4d), suggesting the dominant faradaic effect at a large scan rate. The capacitance contribution percentage of 84.7% in PVSF-2/1 is higher than those of 63.2%, 80.8%, and 72.4% for the PVSF-3/1, PVSF-4/1 and PVSF-5/1 cathodes at 0.6 mV s^{-1} (Figure S12), demonstrating that regulating the vanadium heterovalent ratios of PVSF to reach the optimal heterovalent balance of V^{5+}/V^{4+} contributes to excellent rate performances. This may be ascribed to the reason that the petals of flower-shaped PVSF are stacked by two-dimensional nanosheets, forming a uniform hierarchical structure, which provides a short Zn^{2+} diffusion pathway and fast Zn^{2+} diffusion kinetics.[50] Figure 4e displays the CV profiles of the PVSF with various heterovalent ratios electrodes at 0.2 mV s^{-1}. In contrast to both PVSF-3/1 and PVSF-4.5/1, PVSF-2/1, with a larger peak area, was measured and proven to have a lower polarization voltage (135 mV) than those of PVSF-3/1 (164 mV) and PVSF-4.5/1 (196 mV), which reflects excellent reaction reversibility.[51] The lower polarization voltage of PVSF-2/1 is attributed to the charge density distribution change of the V-O lattice layer by regulating the vanadium heterovalent state, which can achieve high surface reactivity and electrode reaction kinetics, thus reducing the diffusion energy barrier of Zn^{2+}.[40,44]

The reaction kinetics were further illustrated by the galvanostatic intermittent titration technique (GITT) and electrochemical impedance spectroscopy (EIS). The diffusion coefficients ($D_{Zn}{}^{2+}$) of the Zn^{2+} in PVSF with different heterovalent ratios were estimated via GITT. Figures 4f and S14a−d show the GITT charge−discharge curves of PVSF electrodes, and the whole testing process was controlled at a constant current of 0.2 A g^{-1} for a pulse time of 5 min, followed by relaxation for 3 h to allow the voltage to reach equilibrium. The calculated $D_{Zn}{}^{2+}$ of PVSF-2/1 ranges from 10^{-9} to 10^{-10} cm^2 s^{-1} (Figures 4g and S14a), which is higher than the $D_{Zn}{}^{2+}$ values in PVSF-3/1 (10^{-12}−10^{-13} cm^2 s^{-1}), PVSF-4.5/1 (10^{-12}−10^{-13} cm^2 s^{-1}), PVSF-100 (10^{-12}−10^{-14} cm^2 s^{-1}) (Figure S14b, c) and other VOMs, such as VOH (10^{-10}−10^{-11} cm^2 s^{-1}), G-VOH (10^{-10}−10^{-11} cm^2 s^{-1}), and KNVO (10^{-11}−10^{-13} cm^2 s^{-1}).[17,52,53] The fast kinetics of the PVSF-2/1 cathode achieved rapid Zn^{2+} migration, ensuring the adsorption and desorption process of Zn^{2+} during the insertion/extraction reaction process. The heterovalent balance of the V^{5+}/V^{4+} concentration can be conductive to the formation of the electric field in PVSF-2/1. Under the electric field force, Zn^{2+} easily tends to migrate and diffuse in flower-shaped PVSF-2/1. In order to evaluate the electrochemical reaction kinetics property for PVSF-2/1, the Nyquist plots from the EIS analysis of the PVSF-2/1 electrode are also provided in Figure S14e. Before cycling, the R_{ct} of the pristine PVSF-2/1 electrode is about 155 Ω, and the value of Rct in PVSF-2/1 decreases to 74.7 Ω and 53.9 Ω, after 5 and 50 cycles, respectively. The obvious decrease in R_{ct} after the cycles originates from PVSF-2/1 electrode activation. Controlling the V^{5+}/V^{4+} heterovalent ratio to 2:1 can improve the charge density distribution of the V-O layer in PVSF-2/1, providing more charge transfer channels and improving electron transfer during insertion/extraction.[54]

Combined with the above analysis, the excellent properties of PVSF-2/1 can be attributed to heterovalent balance of PVSF-2/1 that the structural pathways corresponding to V^{5+} valence work as Zn^{2+} transport channels to increase Zn^{2+} transport capability, and the V^{4+} valence causes the high charge density distribution of the V-O lattice layer to provide rich active sites for the adsorption and desorption process of Zn^{2+}.

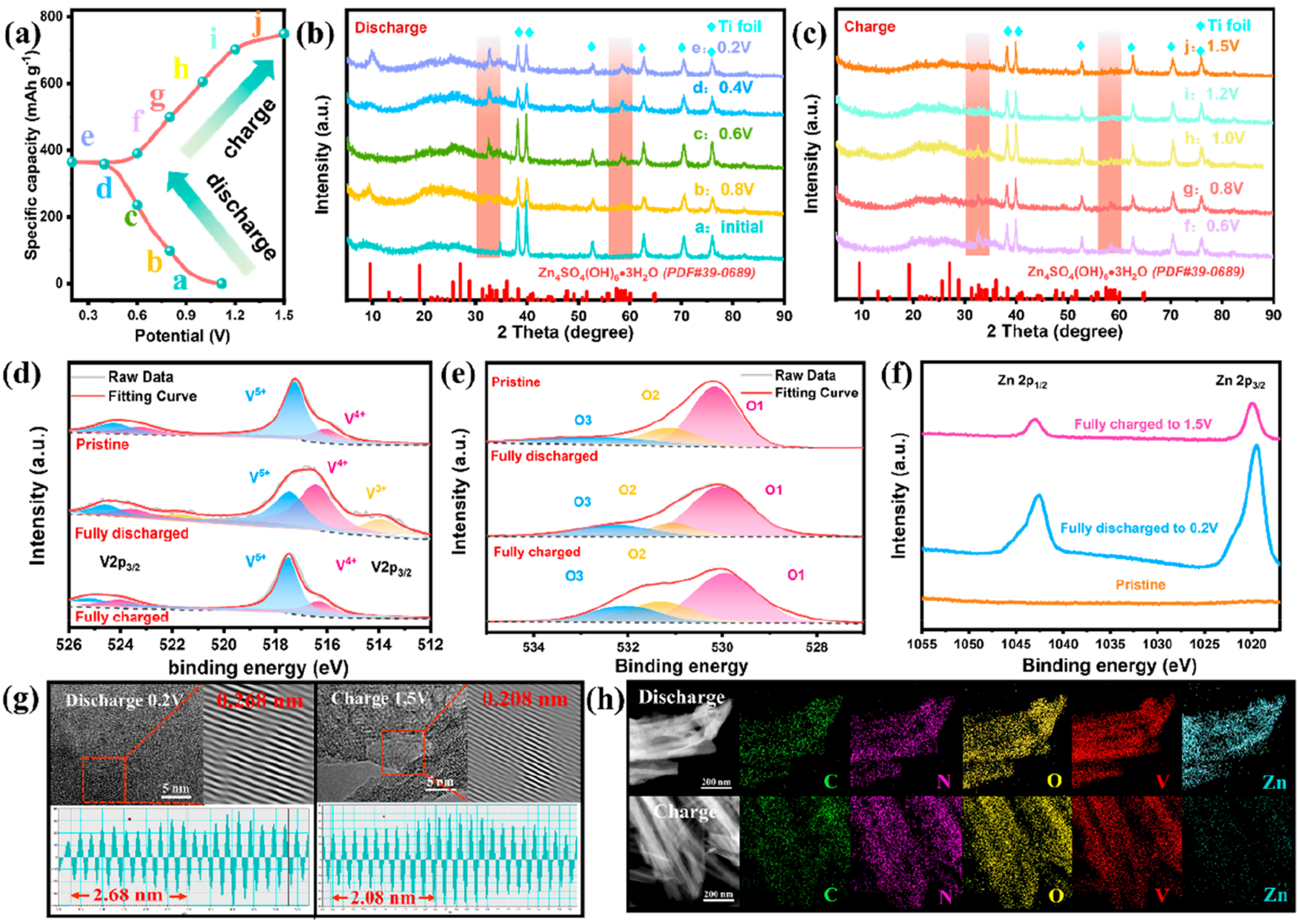

Figure 5. (a) Typical discharge/charge curve in the first operation cycle at 0.2 A g^{-1}. Ex-situ XRD patterns of the PVSF-2/1 cathode at (b) discharge and (c) charge states. XPS spectra of (d)V 2p, (e) O 1s, and (f) Zn 2p regions at the pristine, first discharged (0.2 V), and first charged (1.5 V) states. (g) Ex-situ HRTEM images at fully discharged state and fully charged state. (h) STEM-EDS element mapping images of PVSF-2/1 electrode at discharge/charge states, respectively.

Moreover, the equilibrium of V^{5+}/V^{4+} heterovalent states forms an electric field in PVSF-2/1, ensuring rapid Zn^{2+} migration.[53]

To further demonstrate regulating the role of V^{5+} and V^{4+} heterovalent states for the electrochemical performance of ZIBs cathodes, we prepared a mixed-valence cathode by mixing VO_2 and V_2O_5 materials with a quality ratio of 1:2 (Labeled as VO_2/V_2O_5 = 1/2). The long-cycling performance of the three VO_2, VO_2/V_2O_5, V_2O_5 materials at 5 A g^{-1} was evaluated (Figure S15). The results demonstrate that VO_2 has the highest specific capacity, which suggests that V^{4+} valence provides abundant active sites to boost Zn^{2+} electrochemistry activity in ZIBs. Moreover, the HOMO/LUMO energies and energy gaps (ΔE) were calculated for VO_2 (V^{4+}) and V_2O_5 (V^{5+}). In general, the HOMO energy can be used to reflect the ability to release electrons. The low LUMO energy means it is easier to receive electrons. An "energy gap" is used to determine whether a molecule is easily excited or not. The smaller "energy gap" demonstrates that the closer energy distribution of electrons in molecules is more likely to undergo chemical reactions.[55] We conclude that the energy gap of V_2O_5 is 0.992 eV, much higher than that of VO (0.780 eV), indicating the superior chemical stability of V_2O_5 compared to VO_2 (Figure S14f). This result demonstrates that PVSF with the controlled V^{5+}/V^{4+} heterovalent states ratios ensures maximum electrochemical performance by combining the advantages of $V^{5+}$and V^{4+}.

To investigate the reasons of the enhanced intrinsic activity and the rapid kinetics of PVSF with different heterovalent ratios toward ZIBs, ultraviolet photoelectron spectroscopy (UPS) was performed on PVSF materials. Figure 4h shows that the valence band maximum values of PVSF-2/1, PVSF-3/1, PVSF-4.5/1 and PVSF-100 are calculated to be 2.56, 2.59, 2.63, and 2.48 eV, respectively. Controlling vanadium heterovalent states ratios in the PVSF-2/1 cathode shifts the valence band toward the Fermi level, demonstrating that the excited electrons easily participate in the oxygen reduction electrochemical reaction.[29] The work function (Φ) values of PVSF-2/1, PVSF-3/1, PVSF-4.5/1 and PVSF-100 are 7.54, 7.66, 7.73, and 7.75 eV, respectively. It can be further demonstrated that the occupied V orbital arising from the regulating heterovalent ratio is more conducive to electron migration.[56] Figure 4i shows the Raman spectra of PVSF with different heterovalent ratios. The bending vibration response of the -O-V-O-V- peak appears at 143 cm^{-1}, and the bending vibration response of the V=O peak is located at 268 cm^{-1}. The V_3-O and V_2-O stretching vibrations respond at 524 and 700 cm^{-1}, respectively. A distinct peak at 993 cm^{-1} corresponds to the vibration response of the terminal V=O peak.[26,57] A detailed comparison of the V^{5+} and V^{4+} contents in

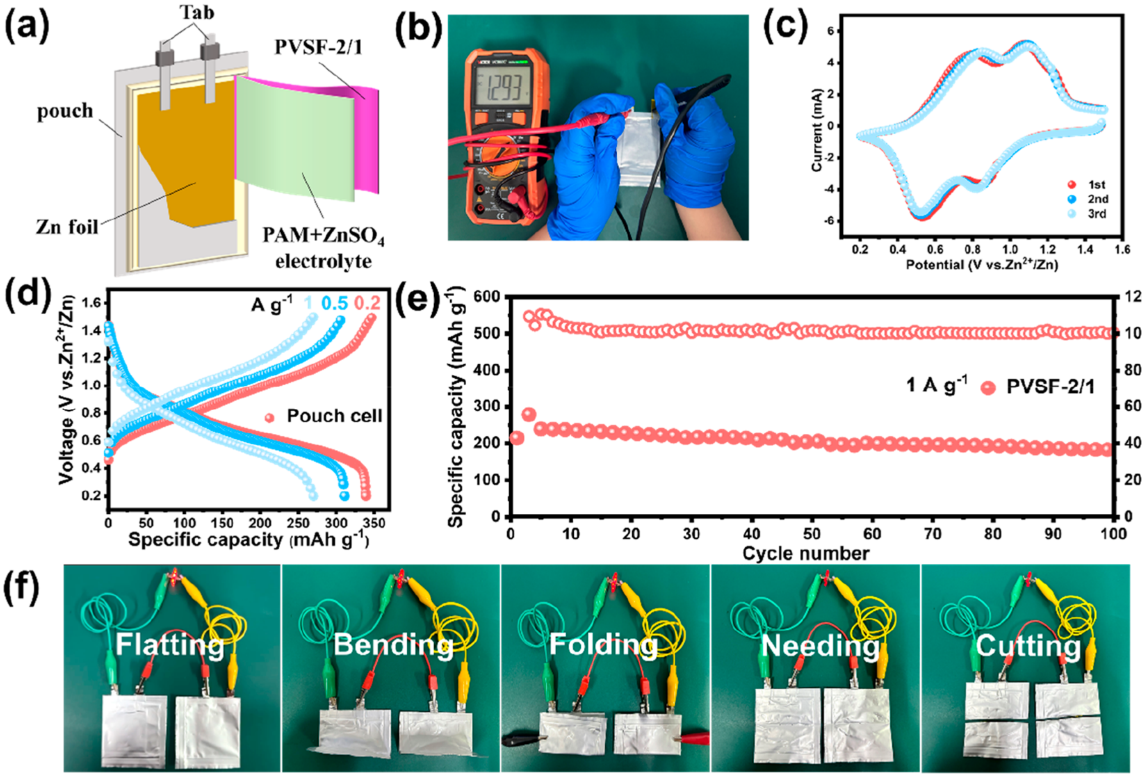

Figure 6. (a) Schematic diagram of the full ZIBs using a PVSF-2/1 cathode, PAM/$ZnSO_4$ electrolyte, and Zn foil anode. (b) Open-circuit voltage. (c) CV curves at the scan rate of 0.1 mV s^{-1} for the Zn||PVSF-2/1 pouch cell. (d) Corresponding GCD curves for the pouch cell at 0.2 A g^{-1}. (e) Cycling performance of the pouch cell with the PVSF-2/1 cathode at 1.0 A g^{-1}. (f) Photographs of open-circuit voltage and lit LED lamps under extreme conditions.

PVSF reveals that the matching peaks of -O-V-O-V-, V_2-O, and V═O show a slight high-shift with controlling vanadium heterovalent ratios from the PVSF-2/1 to PVSF-100 cathode, indicating that the controlling vanadium heterovalent ratios affect the lattice changes. The above results indicate that the V-O lattice structure of the PVSF materials is altered by controlling the vanadium heterovalent ratios, which may further change the distribution of the V-O lattice layer.[58] Thus, the change of the charge density distribution of the V-O lattice layer by controlling the heterovalent states can achieve high surface reactivity and enhance the electrode reaction kinetics.[42]

To explore the charge-storage mechanism of the PVSF-2/1 electrode, a combination of ex-situ XRD, ex-situ XPS, and TEM characterizations were explored in the electrochemical process. Figure 5a reveals the typical GCD profiles of the PVSF-2/1 electrode for the first cycle at 0.2 A g^{-1}, where the labeled states (a−j) were selected for the ex-situ XRD experiment (Figure 5b, c). The diffraction peak of the (001) plane in PVSF-2/1 located at 9.83° shifts slightly to a lower angle at a full discharge of 0.2 V, implying an increase of lattice spacing, and Zn^{2+} was gradually inserted to the V-O lattice (Figure 5b). As charging proceeded to 1.5 V, the (001) diffraction peak returns to the original state with the extraction of Zn^{2+} in the host material, indicating the reversible crystal structure of the PVSF-2/1 cathode during the Zn^{2+} insertion/extraction evolution (Figure 5c).[41] Meanwhile, two new peaks located at 32.75° and 58.35° gradually emerged (Figure 5b) and were identified as $Zn_4SO_4(OH)_6·3H_2O$ (*PDF#39-0689*), which is formed on the PVSF-2/1 cathode surface during the discharge to 0.2 V. The formation of $Zn_4SO_4(OH)_6·3H_2O$ is attributed to H^+ cations intercalated into the V-O lattice, resulting in a PH value increase at the cathode interface.[59] After charging to 1.5 V, two new peaks of $Zn_4SO_4(OH)_6·3H_2O$ gradually disappeared, indicating that the simultaneous H^+ insertion/extraction accompanied during the Zn^{2+} insertion/extraction leads to the formation of the reversible $Zn_4SO_4(OH)_6·3H_2O$ phase at the cathode interface. To further characterize the charge storage mechanism of the PVSF-2/1 electrode, a pair of redox peaks were observed in CV profiles at both 0.1 M acetic acid/anhydrous acetonitrile electrolyte and 0.25 M $Zn(CF_3SO_3)_2$/anhydrous acetonitrile electrolyte at 0.1 mV s^{-1} (Figure S16b, d).[43] This demonstrates the H^+ and Zn^{2+} intercalations of the PVSF-2/1 electrode. Figure S16a, c shows that the two electrolytes achieve stable cycling at 5.0 A g^{-1}, and their specific capacities reach 120 and 115 mAh g^{-1}, respectively. Both H^+ and Zn^{2+} intercalations of PVSF-2/1 anodes can provide capacity, and the capacity of the PVSF-2/1 electrode is provided by the H^+/Zn^{2+} synergistic co-insertion mechanism.

XPS spectra were also used to detect the valence state change of elements during the charge and discharge cycles (Figure 5d−f). As shown in Figure 5d, it is concluded that the intensity of V^{5+} decreased significantly when the cell discharged to 0.2 V, and a new characteristic peak of V^{3+} appeared at 513.8 eV. The results indicate that the pristine V^{5+}/V^{4+} of the PVSF-2/1 cathode was partially reduced to V^{4+}/V^{3+} during the Zn^{2+} insertion process.[60,61] Upon fully charging to 1.5 V, V^{4+} and V^{3+} were reversibly oxidized to V^{5+}. The changes of vanadium valence state are understandable for the insertion/extraction of H^+/Zn^{2+} into the PVSF-2/1 layers. The XPS spectrum of O 1s (Figure 5e) showed that the O2 peak intensity decreased significantly after fully discharging to 0.2 V, proving a decrease in the oxygen vacancy content. It is also verified that the oxygen vacancy could be filled by the insertion of H^+/Zn^{2+}.[62] It is recovered again during the charging process. The increased peak intensity of O3 during charging/discharging probably is ascribed to the insertion of $[Zn(H_2O)_6]^{2+}$ into the V-O lattice, and residual H_2O molecules will remain between the lattice interlayers in the form of crystalline water.[17] As shown in Figure 5f, no signal for the Zn element could be found in the pristine state. After the discharging state reached to 0.2 V, the Zn 2p spectrum shows two peak signals located at 1019.6 and 1042.6 eV, respectively, confirming successful Zn^{2+} insertion. A weak signal peak of Zn element at 1.5 V was caused by a small amount of Zn in the PVSF-2/1, the phenomenon originates from the residue of Zn in the host lattice that may act as pillars for the subsequent stable structure.[63]

HRTEM images of the PVSF-2/1 electrode at the fully discharged/charged state (0.2/1.5 V) exhibit the lattice spacings of 0.268 and 0.208 nm, respectively (Figure 5g), which is in good agreement with ex-situ XRD patterns. The STEM-EDS mapping images visibly reveal the homogeneous dispersion of the C, N, V, O, and Zn elements in the fully discharged PVSF-2/1 nanosheet petal, implying the successful Zn^{2+} insertion. After charging, a weak Zn signal originates from the existence of retained Zn^{2+} in the PVSF-2/1 lattice (Figure 5h), consistent with the ex-situ XPS results. Thus, TEM and EDS analysis results also confirm the reversible Zn^{2+} storage in the PVSF-2/1 electrode.

As for extension of the material's application, quasi-solid-state pouch-type cells were assembled using the PVSF-2/1 cathode, PAM/$ZnSO_4$ hydrogel electrolyte, and Zn foil anode (Figure 6a). The open-circuit voltage of the Zn||PVSF-2/1 pouch cell (4 cm × 4 cm) is stabilized at 1.293 V (Figure 6b). Figure 6c shows the CV profiles at 0.1 mV s^{-1}. Obviously, the two prominent redox peaks are the same as those of coin-type ZIBs. The discharge specific capacity of the Zn||PVSF-2/1 full cell in PAM hydrogel electrolyte is as high as 339 mAh g^{-1} at 0.2 A g^{-1} (Figure 6d), which is higher than those of other VOMs, such as VO_2 (180 mAh g^{-1} at 0.2 A g^{-1}),[64] V_2C/V_2O_5 (60 mAh g^{-1} at 0.2 A g^{-1}),[65] VS_2 (175 mAh g^{-1} at 0.2 A g^{-1}),[63] and 3D-NVO (320 mAh g^{-1} at 0.2 A g^{-1}).[27] The cell also delivers the discharge specific capacity of 250 mAh g^{-1} (Figure 6e) with ~76% capacity retention after 100 cycles at 1.0 A g^{-1}. The properties of Zn||PVSF-2/1 pouch cells are comparable or superior to those of other reported quasi-solid-state pouch-type batteries based on specific capacity (Table S5). The Zn||PVSF-2/1 pouch cell can successfully power a light-emitting diode under different extreme conditions (Figure 6f). These results indicate that the Zn||PVSF-2/1 pouch cell holds a feasible application in energy storage devices.

4. CONCLUSION

We prepared vanadium-supramolecular flower-shaped materials by combining NH_4VO_3 and $C_6H_{12}N_4$. The PVSF with heterovalent V^{5+}/V^{4+} ratios was obtained by presintering etching modification. When the V^{5+}/V^{4+} ratio in PVSF is controlled at 2:1, the obtained PVSF-2/1 material exhibits outstanding electrochemical properties as a cathode material for aqueous ZIBs. The PVSF-2/1 cathode demonstrated a high specific capacity of 398.9 mAh g^{-1} at 0.2 A g^{-1}, excellent rate capability, and outstanding cycling stability. Experimental data reveal that the superior performance of PVSF-2/1 is ascribed to the heterovalent balance of PVSF-2/1 that the structural pathways corresponding to V^{5+} valence work as Zn^{2+} transport channels to increase Zn^{2+} transport capability and V^{4+} valence causes the high charge density distribution of the V-O lattice layer to provide rich active sites for the adsorption and desorption process of Zn^{2+}. The unique flower-shaped PVSF-2/1 contributes to the efficient charge transfer and high ion diffusion ability ($D_{Zn^{2+}} = 10^{-9}-10^{-10}$ cm^2 s^{-1}). The storage mechanism brought by PVSF-2/1 was revealed to be a H^+/Zn^{2+} co-insertion mechanism. The Zn||PVSF-2/1 pouch cells were assembled, which can sustain a high specific capacity of 339 mAh g^{-1} at 0.2 A g^{-1} and successfully power a light-emitting diode under different extreme conditions. Controlling vanadium heterovalent ratios is promising for the development of high-performance, large-scale ZIBs cathode materials.

■ ASSOCIATED CONTENT

Supporting Information

The Supporting Information is available free of charge at https://pubs.acs.org/doi/10.1021/acsami.4c16336.

> Synthesis mechanism diagram of PVSF materials; Physical characterization of VSF and PVSF materials; V 2p spectra of the VSF and PVSF materials; O 1s spectra of the VSF and PVSF materials; EPR spectra of the VSF and PVSF materials; SEM images of the VSF and PVSF materials; EDS spectra of the PVSF-2/1 materials; SEM images of PVSF materials; BET images of PVSF-2/1 materials; Electrochemical characterization of PVSF materials; The capacitive contributions of PVSF materials; The CV curves with capacity separation of PVSF materials; The dQ/dV curves of PVSF materials; Calculation of Zn^{2+} diffusion coefficient of PVSF materials; XPS spectra and Electrochemical characterization of VO_2 and V_2O_5; Electrochemical performance of PVSF-2/1 electrode in different electrolyte; Relative contents tables of V 2p and O 1s for PVSF-2/1; Summary of surface properties; Comparison of electrochemical properties; The quasi-solid-state pouch-type cells performance comparison (PDF)

■ AUTHOR INFORMATION

Corresponding Author

Chengguo Sun − *School of Chemical Engineering, University of Science and Technology Liaoning, Anshan 114051, China; School of Chemical Engineering, Nanjing University of Science and Technology, Nanjing 210094, China;* orcid.org/0000-0003-3580-2153; Email: sunyangguo2004@163.com

Authors

Yue Lu − *School of Chemical Engineering, University of Science and Technology Liaoning, Anshan 114051, China*

Siyang Han − *School of Chemical Engineering, University of Science and Technology Liaoning, Anshan 114051, China*

Jingang Zheng − *School of Chemical Engineering, University of Science and Technology Liaoning, Anshan 114051, China*

Hongwei Zhao − *School of Chemical Engineering, University of Science and Technology Liaoning, Anshan 114051, China*

Han Zhang − *School of Chemical Engineering, University of Science and Technology Liaoning, Anshan 114051, China;* orcid.org/0000-0001-6905-0952

Guangshen Jiang − *School of Chemical Engineering, University of Science and Technology Liaoning, Anshan 114051, China;* orcid.org/0000-0001-9213-1515
Lixiang Li − *School of Chemical Engineering, University of Science and Technology Liaoning, Anshan 114051, China*
Weimin Zhou − *School of Chemical Engineering, University of Science and Technology Liaoning, Anshan 114051, China*
Baigang An − *School of Chemical Engineering, University of Science and Technology Liaoning, Anshan 114051, China;* orcid.org/0000-0001-6111-8166

Complete contact information is available at: https://pubs.acs.org/10.1021/acsami.4c16336

Author Contributions

Yue Lu: Data curation, Investigation, Methodology, Writing − original draft. Siyang Han: Data curation, Investigation. Jingang Zheng: Software, Visualization. Hongwei Zhao: Visualization, Software. Han Zhang: Funding acquisition, Investigation. Guangshen Jiang: Data curation, Visualization. Lixiang Li: Conceptualization, Resources. Weimin Zhou: Conceptualization, Software. Baigang An: Supervision, Funding acquisition, Writing − review and editing. Chengguo Sun: Funding acquisition, Project administration, Supervision, Writing − review and editing.

Notes

The authors declare no competing financial interest.

■ ACKNOWLEDGMENTS

The authors gratefully acknowledge financial support by the National Natural Science Foundation of China (11972178, 21701077, 51972156 and 22109061), the Talent Project of Revitalizing Liaoning (2020LNQN17) and Technology Liaoning Project Grants (601010326).

■ REFERENCES

(1) Zampardi, G.; La Mantia, F. Open Challenges and Good Experimental Practices in the Research Field of Aqueous Zn-Ion Batteries. *Nat. Commun.* **2022**, *13* (1), 687.

(2) Chen, X.; Zhang, H.; Liu, J.-H.; Gao, Y.; Cao, X.; Zhan, C.; Wang, Y.; Wang, S.; Chou, S.-L.; Dou, S.-X. Vanadium-based Cathodes for Aqueous Zinc-Ion Batteries: Mechanism, Design Strategies and Challenges. *Energy Storage Mater.* **2022**, *50*, 21−46.

(3) Zong, Q.; Wu, Y.; Liu, C.; Wang, Q.; Zhuang, Y.; Wang, J.; Tao, D.; Zhang, Q.; Cao, G. Tailoring Layered Transition Metal Compounds for High-Performance Aqueous Zinc-ion Batteries. *Energy Storage Mater.* **2022**, *52*, 250−283.

(4) Chen, D.; Lu, M.; Wang, B.; Chai, R.; Li, L.; Cai, D.; Yang, H.; Liu, B.; Zhang, Y.; Han, W. Uncover the Mystery of High-Performance Aqueous Zinc-Ion Batteries Constructed by Oxygen-doped Vanadium Nitride Cathode: Cationic Conversion Reaction Works. *Energy Storage Mater.* **2021**, *35*, 679−686.

(5) Wang, X.; Xi, B.; Ma, X.; Feng, Z.; Jia, Y.; Feng, J.; Qian, Y.; Xiong, S. Boosting Zinc-Ion Storage Capability by Effectively Suppressing Vanadium Dissolution Based on Robust Layered Barium Vanadate. *Nano Lett.* **2020**, *20* (4), 2899−2906.

(6) Lv, T.; Peng, Y.; Zhang, G.; Jiang, S.; Yang, Z.; Yang, S.; Pang, H. How About Vanadium-Based Compounds as Cathode Materials for Aqueous Zinc Ion Batteries? *Adv. Sci.* **2023**, *10* (12), No. 2206907.

(7) Yi, T.-F.; Qiu, L.; Qu, J.-P.; Liu, H.; Zhang, J.-H.; Zhu, Y.-R. Towards High-Performance Cathodes: Design and Energy Storage Mechanism of Vanadium Oxides-Based Materials for Aqueous Zn-Ion Batteries. *Coord. Chem. Rev.* **2021**, *446*, No. 214124.

(8) Bai, Y.; Qin, Y.; Hao, J.; Zhang, H.; Li, C. M. Advances and Perspectives of Ion-Intercalated Vanadium Oxide Cathodes for High-Performance Aqueous Zinc Ion Battery. *Adv. Funct. Mater.* **2024**, *34*, No. 2310393.

(9) Wang, Z.; Diao, J.; Kawashima, K.; Weeks, J. A.; Vaidyula, R. R.; Marquez, R. A.; Miller, N.; Henkelman, G.; Mullins, C. B. Unveiling the Reaction Mechanism of Capacity Reactivation in Silver Vanadate Cathodes for Aqueous Zinc-Ion Batteries. *J. Mater. Chem. A 11* **2023**, *11*, 18881−18892.

(10) Cao, Z.; Wang, L.; Zhang, H.; Zhang, X.; Liao, J.; Dong, J.; Shi, J.; Zhuang, P.; Cao, Y.; Ye, M. Localized Ostwald Ripening Guided Dissolution/Regrowth to Ancient Chinese Coin-Shaped VO_2 Nanoplates with Enhanced Mass Transfer for Zinc Ion Storage. *Adv. Funct. Mater.* **2020**, *30* (25), No. 2000472.

(11) Cao, Z.; Zhang, H.; Song, B.; Xiong, D.; Tao, S.; Deng, W.; Hu, J.; Hou, H.; Zou, G.; Ji, X. Angstrom-Level Ionic Sieve 2D-MOF Membrane for High Power Aqueous Zinc Anode. *Adv. Funct. Mater.* **2023**, *33*, No. 2300339.

(12) Xiao, X.; Duan, X.; Song, Z.; Deng, X.; Deng, W.; Hou, H.; Zheng, R.; Zou, G.; Ji, X. High-Throughput Production of Cheap Mineral-Based Heterostructures for High Power Sodium Ion Capacitors. *Adv. Funct. Mater.* **2022**, *32* (18), No. 2110476.

(13) Bin, D.; Huo, W.; Yuan, Y.; Huang, J.; Liu, Y.; Zhang, Y.; Dong, F.; Wang, Y.; Xia, Y. Organic-Inorganic-Induced Polymer Intercalation into Layered Composites for Aqueous Zinc-Ion Battery. *Chem.* **2020**, *6* (4), 968−984.

(14) Wang, Y.; Zhang, Y.; Gao, G.; Fan, Y.; Wang, R.; Feng, J.; Yang, L.; Meng, A.; Zhao, J.; Li, Z. Effectively Modulating Oxygen Vacancies in Flower-Like δ-MnO_2 Nanostructures for Large Capacity and High-Rate Zinc-Ion Storage. *Nano Micro Lett.* **2023**, *15* (1), 219.

(15) Li, S.; Wei, X.; Chen, H.; Lai, G.; Wang, X.; Zhang, S.; Wu, S.; Tang, W.; Lin, Z. A Mixed-Valent Vanadium Oxide Cathode with Ultrahigh Rate Capability for Aqueous Zinc-Ion Batteries. *J. Mater. Chem. A* **2021**, *9* (39), 22392−22398.

(16) Liu, F.; Chen, Z.; Fang, G.; Wang, Z.; Cai, Y.; Tang, B.; Zhou, J.; Liang, S. V_2O_5 Nnanospheres with Mixed Vanadium Valences as High Electrochemically Active Aqueous Zinc-Ion Battery Cathode. *Nano Micro Lett.* **2019**, *11*, 1−11.

(17) Zong, Q.; Wang, Q.; Liu, C.; Tao, D.; Wang, J.; Zhang, J.; Du, H.; Chen, J.; Zhang, Q.; Cao, G. Potassium Ammonium Vanadate with Rich Oxygen Vacancies for Fast and Highly Stable Zn-Ion Storage. *ACS Nano* **2022**, *16* (3), 4588−4598.

(18) Cao, J.; Ou, T.; Geng, S.; Zhang, X.; Zhang, D.; Zhang, L.; Luo, D.; Zhang, X.; Qin, J.; Yang, X. Constructing Stable V_2O_5/V_6O_{13} Heterostructure Interface with Fast Zn^{2+} Diffusion Kinetics for Ultralong Lifespan Zinc-Ion Batteries. *Colloid Interface Sci.* **2024**, *656*, 495−503.

(19) Wu, T.; Zhu, K.; Qin, C.; Huang, K. Unraveling the Role of Structural Water in Bilayer V_2O_5 during Zn^{2+}-Intercalation: Insights from DFT Calculations. *J. Mater. Chem. A* **2019**, *7* (10), 5612−5620.

(20) Yang, Y.; Wang, Y.; Zhao, L.; Liu, Y.; Ran, F. Visualizing Nucleation and Growth Process of Vanadium-Supramolecular Nanoribbons Self-Assembled by Rapid Cooling Method towards High-Capacity Vanadium Nitride Anode Materials. *Adv. Energy Mater.* **2022**, *12* (13), No. 2103158.

(21) Lai, S.; Tao, Z.; Cui, J.; Wang, A.; Tan, Y.; Chen, Z.; Yang, Y. A Novel Vanadium Coordination Supramolecular Network with Multiple Active Sites for Ultra-Durable Aqueous Zinc Metal Batteries. *J. Mater. Chem. A* **2023**, *11* (38), 20786−20795.

(22) Zhang, W.; Xiao, Y.; Zuo, C.; Tang, W.; Liu, G.; Wang, S.; Cai, W.; Dong, S.; Luo, P. Adjusting the Valence State of Vanadium in VO_2 (B) by Extracting Oxygen Anions for High-Performance Aqueous Zinc-Ion Batteries. *ChemSusChem* **2021**, *14* (3), 971−978.

(23) Li, X.; Chen, Z.; Ruan, P.; Hu, X.; Yuan, X.; Lu, B.; Qin, L.; Zhou, J. Guiding Uniform Zn Deposition with a Multifunctional Additive for Highly Utilized Zn Anodes. *Nanoscale.* **2024**, *16*, 18835−18842.

(24) Li, J.; Liu, Z.; Han, S.; Zhou, P.; Lu, B.; Zhou, J.; Zeng, Z.; Chen, Z.; Zhou, J. Hetero Nucleus Growth Stabilizing Zinc Anode for High-Biosecurity Zinc-Ion Batteries. *Nano-Micro Letters* **2023**, *15* (1), 237.

(25) Barrio, J.; Grafmüller, A.; Tzadikov, J.; Shalom, M. Halogen-Hydrogen Bonds: A General Synthetic Approach for Highly Photoactive Carbon Nitride with Tunable Properties. *Appl. Catal., B* **2018**, *237*, 681−688.

(26) Zhang, J.; Wang, M.; Zeng, M.; Li, X.; Chen, L.; Yang, Z.; Chen, J.; Guo, B.; Ma, Z.; Li, X. Sulfite Modified and Ammonium Ion Intercalated Vanadium Hydrate with Enhanced Redox Kinetics for Aqueous Zinc Ion Batteries. *J. Power Sources* **2021**, *496*, No. 229832.

(27) Li, Q.; Rui, X.; Chen, D.; Feng, Y.; Xiao, N.; Gan, L.; Zhang, Q.; Yu, Y.; Huang, S. A High-Capacity Ammonium Vanadate Cathode for Zinc-Ion Battery. *Nano Micro Lett.* **2020**, *12*, 1−12.

(28) Li, H.; Yang, J.; Cheng, J.; He, T.; Wang, B. Flexible Aqueous Ammonium-Ion Full Cell with High Rate Capability and Long Cycle Life. *Nano Energy* **2020**, *68*, No. 104369.

(29) Du, Y.; Wang, X.; Sun, J. Tunable Oxygen Vacancy Concentration in Vanadium Oxide as Mass-Produced Cathode for Aqueous Zinc-Ion Batteries. *Nano Res.* **2021**, *14*, 754−761.

(30) Tan, Q.; Li, X.; Zhang, B.; Chen, X.; Tian, Y.; Wan, H.; Zhang, L.; Miao, L.; Wang, C.; Gan, Y. Valence Engineering via In Situ Carbon Reduction on Octahedron Sites Mn_3O_4 for Ultra-Long Cycle Life Aqueous Zn-Ion Battery. *Adv. Energy Mater.* **2020**, *10* (38), No. 2001050.

(31) Wu, L.; Fu, H.; Lyu, W.; et al. Rational Regulation of High-Voltage Stability in Potassium Layered Oxide Cathodes[J]. *ACS Nano* **2024**, *18*, 13415−13427.

(32) Wu, L.; Li, S.; Li, L.; Zhang, H.; Tao, L.; Geng, X.; Yang, H.; Zhou, W.; Sun, C.; Ju, D. Modest Modulation on the Electronic Structure of Co_9S_8 by Vanadium Doping for High-Performance Rechargeable Zn−Air Batteries. *Appl. Catal., B* **2023**, *324*, No. 122250.

(33) Li, Z.; Ren, Y.; Mo, L.; Liu, C.; Hsu, K.; Ding, Y.; Zhang, X.; Li, X.; Hu, L.; Ji, D. Impacts of Oxygen Vacancies on Zinc Ion Intercalation in VO_2. *ACS Nano* **2020**, *14* (5), 5581−5589.

(34) Wang, B.; Huang, Y.; Han, Y.; Zhang, W.; Zhou, C.; Jiang, Q.; Chen, F.; Wu, X.; Li, R.; Lyu, P. A Facile Strategy To Construct Au@ $V_xO_{2\ x+1}$ Nanoflowers as a Multicolor Electrochromic Material for Adaptive Camouflage. *Nano Lett.* **2022**, *22* (9), 3713−3720.

(35) Zhang, Y.; Li, Z.; Liu, M.; Liu, J. Construction of Novel Polyaniline-Intercalated Hierarchical Porous V_2O_5 Nanobelts with Enhanced Diffusion Kinetics and Ultra-Stable Cyclability for Aqueous Zinc-Ion Batteries. *Chem. Eng. J.* **2023**, *463*, No. 142425.

(36) Chen, H.; Huang, J.; Tian, S.; Liu, L.; Qin, T.; Song, L.; Liu, Y.; Zhang, Y.; Wu, X.; Lei, S. Interlayer Modification of Pseudocapacitive Vanadium Oxide and Zn (H_2O) n^{2+} Migration Regulation for Ultrahigh Rate and Durable Aqueous Zinc-Ion Batteries. *Adv. Sci.* **2021**, *8* (14), No. 2004924.

(37) He, T.; Weng, S.; Ye, Y.; Cheng, J.; Wang, X.; Wang, X.; Wang, B. Cation-Deficient $Zn_{0.\ 3}$ $(NH_4)_{\ 0.3}$ V_4O_{10}• 0.91 H_2O for Rechargeable Aqueous Zinc Battery with Superior Low-Temperature Performance. *Energy Storage Mater.* **2021**, *38*, 389−396.

(38) Wang, D.; Wang, L.; Liang, G.; Li, H.; Liu, Z.; Tang, Z.; Liang, J.; Zhi, C. A Superior δ-MnO_2 Cathode and a Self-Healing Zn-δ-MnO_2 Battery. *ACS Nano* **2019**, *13* (9), 10643−10652.

(39) Zhao, J.; Ren, H.; Liang, Q.; Yuan, D.; Xi, S.; Wu, C.; Manalastas, W., Jr; Ma, J.; Fang, W.; Zheng, Y. High-Performance Flexible Quasi-Solid-State Zinc-Ion Batteries with Layer-Expanded Vanadium Oxide Cathode and Zinc/Stainless Steel Mesh Composite Anode. *Nano Energy* **2019**, *62*, 94−102.

(40) Shi, W.; Yin, B.; Yang, Y.; Sullivan, M. B.; Wang, J.; Zhang, Y.-W.; Yu, Z. G.; Lee, W. S. V.; Xue, J. Unravelling V_6O_{13} Diffusion Pathways via CO_2 Modification for High-Performance Zinc Ion Battery Cathode. *ACS Nano* **2021**, *15* (1), 1273−1281.

(41) Cao, H.; Zheng, Z.; Norby, P.; Xiao, X.; Mossin, S. Electrochemically Induced Phase Transition in $V_3O_7{\cdot}H_2O$ Nanobelts/Reduced Graphene Oxide Composites for Aqueous Zinc-Ion Batteries. *Small* **2021**, *17* (24), No. 2100558.

(42) Li, G.; Yang, Z.; Jiang, Y.; Jin, C.; Huang, W.; Ding, X.; Huang, Y. Towards Polyvalent Ion Batteries: a Zinc-Ion Battery Based on NASICON Structured Na_3V_2 $(PO_4)_3$. *Nano Energy* **2016**, *25*, 211−217.

(43) Zhu, K.; Wei, S.; Shou, H.; Shen, F.; Chen, S.; Zhang, P.; Wang, C.; Cao, Y.; Guo, X.; Luo, M.; Zhang, H.; Ye, B.; Wu, X.; He, L.; Song, L. Defect Engineering on V_2O_3 Cathode for Long-Cycling Aqueous Zinc Metal Batteries. *Nat. Commun.* **2021**, *12*, 6878.

(44) Zhang, F.; Du, M.; Miao, Z.; Li, H.; Dong, W.; Sang, Y.; Jiang, H.; Li, W.; Liu, H.; Wang, S. Oxygen Vacancies and N-doping in Organic−Inorganic Pre-Intercalated Vanadium Oxide for High-Performance Aqueous Zinc-Ion Batteries. *InfoMat* **2022**, *4* (11), No. e12346.

(45) Zhang, G.; Wu, T.; Zhou, H.; Jin, H.; Liu, K.; Luo, Y.; Jiang, H.; Huang, K.; Huang, L.; Zhou, J. Rich Alkali Ions Preintercalated Vanadium Oxides for Durable and Fast Zinc-Ion Storage. *ACS Energy Lett.* **2021**, *6* (6), 2111−2120.

(46) Liu, Y.; Hu, P.; Liu, H.; Wu, X.; Zhi, C. Tetragonal VO_2 Hollow Nanospheres as Robust Cathode Material for Aqueous Zinc Ion Batteries. *Today Energy* **2020**, *17*, No. 100431.

(47) Javed, M. S.; Lei, H.; Wang, Z.; Liu, B.-t.; Cai, X.; Mai, W. 2D V_2O_5 Nanosheets as a Binder-Free High-Energy Cathode for Ultrafast Aqueous and Flexible Zn-Ion Batteries. *Nano Energy* **2020**, *70*, No. 104573.

(48) Hong, J.; Xie, L.; Shi, C.; Lu, X.; Shi, X.; Cai, J.; Wu, Y.; Shao, L.; Sun, Z. High-Performance Aqueous Zinc-Ion Batteries Based on Multidimensional V_2O_3 Nanosheets@ Single-Walled Carbon Nanohorns@ Reduced Graphene Oxide Composite and Optimized Electrolyte. *Small Methods* **2024**, *8*, No. 2300205.

(49) Qiu, N.; Yang, Z.; Xue, R.; Wang, Y.; Zhu, Y.; Liu, W. Toward a High-Performance Aqueous Zinc Ion Battery: Potassium Vanadate Nanobelts and Carbon Enhanced Zinc Foil. *Nano Lett.* **2021**, *21* (7), 2738−2744.

(50) Chen, H.; Rong, Y.; Yang, Z.; Deng, L.; Wu, J. V_2O_3@ Amorphous Carbon as a Cathode of Zinc Ion Batteries with High Stability and Long Cycling Life. *Ind. Eng. Chem. Res.* **2021**, *60* (4), 1517−1525.

(51) Hao, J.; Li, B.; Li, X.; Zeng, X.; Guo, Z. An In-Depth Study of Zn Metal Surface Chemistry for Advanced Aqueous Zn-Ion Batteries. *Adv. Mater.* **2020**, *32* (34), No. 2003021.

(52) Zhang, N.; Jia, M.; Dong, Y.; Wang, Y.; Xu, J.; Liu, Y.; Jiao, L.; Cheng, F. Hydrated Layered Vanadium Oxide as a Highly Reversible Cathode for Rechargeable Aqueous Zinc Batteries. *Adv. Funct. Mater.* **2019**, *29* (10), No. 1807331.

(53) Zhang, J.; Wang, M.; Zhong, J.; Wang, X.; Huang, X.; Yang, Z.; Chen, J.; Guo, B.; Ma, Z.; Li, X. Gradient Valence-Distributed Vanadium Oxygen Hydrate Hybrid Induces High Performance Aqueous Zinc-Ion Batteries. *Mater. Chem. Front.* **2021**, *5* (20), 7518−7528.

(54) Liu, W.; Dong, L.; Jiang, B.; Huang, Y.; Wang, X.; Xu, C.; Kang, Z.; Mou, J.; Kang, F. Layered Vanadium Oxides with Proton and Zinc Ion Insertion for Zinc Ion Batteries. *Electrochim. Acta* **2019**, *320*, No. 134565.

(55) Ye, Z.; Xie, S.; Cao, Z.; Wang, L.; Xu, D.; Zhang, H.; Matz, J.; Dong, P.; Fang, H.; Shen, J. High-Rate Aqueous Zinc-Organic Battery Achieved by Lowering HOMO/LUMO of Organic Cathode. *Energy Storage Mater.* **2021**, *37*, 378−386.

(56) Wang, Y.; Wei, S.; Qi, Z.-H.; Chen, S.; Zhu, K.; Ding, H.; Cao, Y.; Zhou, Q.; Wang, C.; Zhang, P. Intercalant-Induced Vt_{2g} Orbital Occupation in Vanadium Oxide Cathode Toward Fast-Charging Aqueous Zinc-Ion Batteries. *Proc. Natl. Acad. Sci. U.S.A.* **2023**, *120* (13), No. e2217208120.

(57) Liu, C.; Neale, Z.; Zheng, J.; Jia, X.; Huang, J.; Yan, M.; Tian, M.; Wang, M.; Yang, J.; Cao, G. Expanded Hydrated Vanadate for High-Performance Aqueous Zinc-Ion Batteries. *Energy Environ. Sci.* **2019**, *12* (7), 2273−2285.

(58) Dong, J.; Jiang, Y.; Wei, Q.; Tan, S.; Xu, Y.; Zhang, G.; Liao, X.; Yang, W.; Li, Q.; An, Q. Strongly Coupled Pyridine-V_2O_5 Center dot nH $_{(2)}$ O Nanowires with Intercalation Pseudocapacitance and Stabilized Layer for High Energy Sodium Ion Capacitors. *Small* **2019**, *15* (22), No. 1900379.

(59) Li, R.; Zhang, H.; Zheng, Q.; Li, X. Porous V_2O_5 Yolk−Shell Microspheres for Zinc Ion Battery Cathodes: Activation Responsible for Enhanced Capacity and Rate Performance. *J. Mater. Chem. A* **2020**, *8* (10), 5186−5193.

(60) Geng, H.; Cheng, M.; Wang, B.; Yang, Y.; Zhang, Y.; Li, C. C. Electronic Structure Regulation of Layered Vanadium Oxide via Interlayer Doping Strategy Toward Superior High-Rate and Low-Temperature Zinc-Ion Batteries. *Adv. Funct. Mater.* **2020**, *30* (6), No. 1907684.

(61) Wang, X.; Wang, Y.; Jiang, Y.; Li, X.; Liu, Y.; Xiao, H.; Ma, Y.; Huang, Y. y.; Yuan, G. Tailoring Ultrahigh Energy Density and Stable Dendrite-Free Flexible Anode with $Ti_3C_2T_x$ MXene Nanosheets and Hydrated Ammonium Vanadate Nanobelts for Aqueous Rocking-Chair Zinc Ion Batteries. *Adv. Funct. Mater.* **2021**, *31* (35), No. 2103210.

(62) Liu, Y.; Xiao, X.; Liu, X.; Cui, L. L.; Gong, Y. Aluminium Vanadate with Unsaturated Coordinated V centers and Oxygen Vacancies: Surface Migration and Partial Phase Transformation Mechanism in High Performance Zinc-Ion Batteries. *J. Mater. Chem. A* **2022**, *10* (2), 912−927.

(63) Tan, Y.; Li, S.; Zhao, X.; Wang, Y.; Shen, Q.; Qu, X.; Liu, Y.; Jiao, L. Unexpected Role of the Interlayer "Dead Zn^{2+}" in Strengthening the Nanostructures of VS_2 Cathodes for High Performance Aqueous Zn-Ion Storage. *Adv. Energy Mater.* **2022**, *12* (19), No. 2104001.

(64) Dai, X.; Wan, F.; Zhang, L.; Cao, H.; Niu, Z. Freestanding Graphene/VO_2 Composite Films for Highly Stable Aqueous Zn-ion Batteries with Superior Rate Performance. *Energy Storage Mater.* **2019**, *17*, 143−150.

(65) Cai, P.; Wang, K.; He, X.; Li, Q.; Zhang, Z.; Li, M.; Li, H.; Zhou, M.; Wang, W.; Jiang, K. Electric-field Harmony in V_2C/V_2O_5 Heterointerfaces toward High-Performance Aqueous Zn-Ion Batteries. *Energy Storage Mater.* **2023**, *60*, No. 102835.